Journal of Energy Storage 132 (2025) 117784

Contents lists available at ScienceDirect

Journal of Energy Storage

journal homepage: www.elsevier.com/locate/est

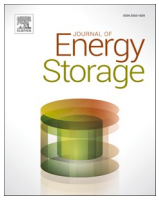

Research papers

Numerical and experimental analysis of triply periodic minimal surface (TPMS)-based metal lattice heat sinks integrated with different phase change materials for enhanced thermal management of electronics

Mohammad Arqam [a], Laryssa Sueza Raffa [a], Matt Ryall [b], Mohammad S. Islam [a], Nick S. Bennett [a,*]

[a] School of Mechanical and Mechatronic Engineering, University of Technology Sydney, Ultimo, NSW 2007, Australia
[b] Mawson Rovers, Eveleigh, NSW 2015, Australia.

ARTICLE INFO

Keywords:
Triply periodic minimal surface (TPMS)
Phase change material (PCM)
Thermal conductivity enhancer (TCE)
Thermal management
Electronics

ABSTRACT

This study investigates the thermal performance of Triply Periodic Minimal Surface (TPMS)-based metal lattice heat sinks integrated with three Phase Change Materials (PCMs): RT55, RT42, and RT31. The objective is to optimize thermal management for high-performance electronics by evaluating the influence of PCM thermal properties and lattice geometry on heat transfer and phase change dynamics. Four TPMS-based designs octahedral (P3), waveform (P2), droplet (P4) and primitive (P6) were numerically analyzed under unidirectional heat flux conditions using a finite volume method. The simulations considered transient base and average temperature profiles, liquid fraction progression, and time to complete melting. Results revealed that primitive design consistently outperformed other configurations, achieving the lowest base temperature of 72 °C with RT31 and completing phase change in just 491 s, 28 % faster than waveform design and over 50 % faster than droplet design. Conversely, droplet design exhibited the slowest thermal response, with a base temperature of 90 °C and a melting time exceeding 3500 s for RT55. Among the PCMs, RT31 demonstrated superior thermal buffering due to its lower melting temperature, stabilizing average temperatures at least 5 °C lower than RT42 and RT55. The study highlights the importance of symmetrical lattice structures, such as in primitive design, for enhancing heat transfer efficiency and reducing phase change duration. This work contributes to advancing TPMS-based heat sink designs and provides actionable insights for integrating PCMs into next-generation thermal management systems for energy storage and electronics cooling.

1. Introduction

Effective thermal management is crucial for the operational reliability and longevity of modern electronics, where nearly half of electronic failures are attributable to thermal issues [1]. With advancements in technology and the miniaturization of devices, heat dissipation challenges have become increasingly significant, particularly in high-power electronics where heat fluxes can reach up to 150 kW/m^2 [2]. The global electronics market faces an estimated annual loss exceeding $1 billion due to overheating-related failures, emphasizing the critical need for innovative cooling solutions [3]. Phase Change Materials (PCMs), known for their high latent heat and near-isothermal heat storage and release properties, have emerged as a promising avenue for addressing these thermal challenges [4,5]. Among these, paraffin-based PCMs are widely recognized for their thermal stability and ease of handling, but their low thermal conductivity (typically 0.1–0.4 W/mK) limits their standalone application [6]. Inorganic PCMs, such as salt hydrates, and metallic PCMs, like gallium, offer superior thermal conductivity but are constrained by challenges related to cost, toxicity, and material compatibility [7,8]. These constraints necessitate innovative composite designs and advanced heat sink configurations incorporating thermal conductivity enhancers to mitigate overheating risks effectively [9].

Cooling methodologies for electronics are broadly categorized into active and passive techniques. Active cooling systems, such as liquid cooling and forced air, are widely employed for their high precision and effectiveness in controlling temperatures under variable loads. However, these systems are often associated with high energy consumption, mechanical complexity, and increased system bulk, making them less

* Corresponding author.
E-mail address: Nicholas.Bennett@uts.edu.au (N.S. Bennett).

https://doi.org/10.1016/j.est.2025.117784
Received 10 April 2025; Received in revised form 23 June 2025; Accepted 16 July 2025
Available online 25 July 2025

Nomenclature

3D	Three dimensional, –
AM	Additive manufacturing, –
C	Mush constant, –
CAD	Computer-Aided Design, –
Cp	Specific heat capacity, J/kg·K
f	Phase change material (liquid), –
FVM	Finite volume method, –
g	Gravitational acceleration, m/s^2
H	Height, mm
HP	Heater power, –
HTC	Heat Transfer Coefficient, W/m^{2}K
ini	Initial, –
k	Thermal conductivity, W/m·K
L	Latent heat of fusion, kJ/kg
l	Liquid, –
m	Mass, kg
M	Million, –
p	Pressure, Pa
PCM	Phase Change Material, –
Q	Heat input, W
ref	Reference, –
S	Source term in momentum equation, –
s	Solid (metal), –
SS	Stainless steel, –
t	Time, s
t_{base}	Base thickness, mm
TCE	Thermal conductivity enhancer, –
TEC	Thermal energy storage, –
t_{fin}	Fin thickness, mm
Ti	Titanium, –
T_{ini}	Initial temperature, °C
T_{liq}	PCM liquidus temperature, °C
TM	Thermal Management, –
TPMS	Triply Periodic Minimal Surface, –
T_{sol}	PCM solidus temperature, °C
t_{wall}	Wall thickness, mm
u	Velocity component in x direction, m/s
v	Velocity component in y direction, m/s
w	Velocity component in z direction, m/s
W	Width, mm
x, y, z	Cartesian coordinates, –
β	Thermal expansion coefficient, 1/K
δ	Small constant to avoid singularities, –
λ	Liquid fraction, –
μ	Dynamic viscosity, kg/m·s
ρ	Density, kg/m^3

viable for compact electronics [2,10]. Passive cooling systems, on the other hand, rely on thermal design efficiency and materials like Phase Change Materials (PCMs) to manage heat. Passive systems, including PCM-based heat sinks, are favoured for their energy independence, simplicity, and ability to maintain near-isothermal conditions during operation [11]. Among the various thermal conductivity enhancers integrated into PCMs, metal foams [13,15,16], fins [12,14,34,35], nanoparticles [17–22], and periodic cellular structures like Triply Periodic Minimal Surfaces (TPMS) have shown significant promise in addressing the intrinsic low thermal conductivity of PCMs [28–30]. For example, TPMS-based designs have demonstrated the ability to enhance PCM melting times by up to 40 % in isothermal applications through effective heat distribution [9]. Similarly, hybrid cooling approaches, where PCM-based passive systems are supplemented by active elements such as fans, have been proposed to manage high-heat fluxes efficiently [23–26]. These advancements emphasize the potential of innovative designs that combine active and passive cooling for improved thermal management in high-performance electronics.

The advent of additive manufacturing (AM) has revolutionized the design and fabrication of complex geometries, enabling the creation of intricate lattice structures with precise control over porosity, cell size, and topology. Triply Periodic Minimal Surfaces (TPMS) structures, such as gyroid, primitive, and IWP, have garnered significant attention for thermal management applications due to their high surface area-to-volume ratios and robust mechanical properties [25–27]. AM techniques, such as selective laser melting (SLM) and electron beam melting (EBM), facilitate the production of these lattices with unprecedented precision, making them ideal for integrating into PCM-based heat sinks [28,29]. Studies have shown that embedding TPMS structures within PCMs significantly enhances heat transfer by mitigating thermal resistance, thus improving the thermal conductivity of the system by up to 13 times compared to PCM alone [28]. Beyond their inherent thermal properties, TPMS lattices offer customization to optimize performance under specific conditions. For instance, functional grading of porosity and wall thickness has been demonstrated to further enhance heat dissipation and storage capacity [4,9]. Material selection plays a critical role, with alloys such as AlSi10Mg and copper showing superior thermal conductivity when used in lattice fabrication [7,30]. Post-processing techniques, such as heat treatment, have also been explored to enhance lattice performance, reducing anisotropy and improving thermal efficiency by over 30 % in some cases [8].

TPMS designs are particularly effective in applications requiring phase-change heat transfer, as their intricate geometries promote natural convection and reduce melting times within PCMs. For example, numerical studies by [5,31] revealed that incorporating TPMS lattices reduced PCM melting times by up to 40 %, with the gyroid and primitive structures showing distinct advantages in buoyancy-enhanced scenarios. Similarly, metallic PCMs, such as gallium, when paired with TPMS lattices, have demonstrated robust performance under high heat fluxes, achieving greater temperature uniformity and reduced thermal hotspots [32]. The flexibility of AM enables the production of TPMS structures with optimized designs tailored for specific cooling applications, such as high-power electronics. Recent studies have highlighted their potential to outperform conventional metal foams by achieving superior heat transfer rates and improved mechanical robustness [6]. These advancements position TPMS-integrated PCMs as a critical innovation in thermal management systems for next-generation electronic devices.

The integration of TPMS lattice structures with various PCMs has been extensively studied, revealing promising synergies between their geometric configurations and thermal management properties. Experimental studies have shown that embedding TPMS structures within PCMs significantly improves heat transfer rates by facilitating enhanced natural convection and conduction pathways [5,10]. For instance, TPMS-based designs, such as gyroid and primitive structures, exhibit distinct thermal characteristics depending on the PCM type, with paraffin-based PCMs benefiting from increased buoyancy-induced convection, while metallic PCMs like gallium excel in pure conduction scenarios [11,28]. In a comparative analysis, Qureshi et al. [6] reported that TPMS structures outperformed conventional metal foams in both isothermal and non-isothermal conditions, highlighting their adaptability across varying heat flux applications.

Advanced numerical simulations have further emphasized the importance of lattice porosity and cell topology in determining PCM melting dynamics. Catchpole-Smith et al. [9] noted that higher porosity lattices facilitated faster melting and reduced temperature gradients within the PCM, which is crucial for maintaining operational stability in

electronic devices. Furthermore, Sélô et al. [8] demonstrated that post-processing treatments, such as heat treatment, can enhance the thermal conductivity of TPMS lattices by eliminating anisotropy, making them more effective for high-heat flux scenarios. Experimental investigations have also explored the role of TPMS lattices in different PCM configurations, such as hybrid PCM systems combining organic and metallic phases. For example, Iradukunda et al. [33] found that hybrid PCM systems embedded within TPMS lattices achieved superior thermal performance, particularly under transient conditions. These findings were corroborated by Ho et al. [29], who observed that lattice structures enabled more uniform temperature distribution across PCM layers, reducing localized overheating and enhancing system reliability.

The integration of TPMS lattices with PCMs has also extended to multi-phase heat sink designs, where lattice geometries are optimized for simultaneous conduction and convection heat transfer. Studies by Al-Ketan et al. [27,30] have explored this potential, showing that TPMS lattices can sustain high thermal loads while minimizing structural weight, making them ideal for aerospace and automotive applications. Moreover, Samson et al. [31] emphasized the role of buoyancy-induced flow patterns within TPMS-PCM systems, revealing that lattice orientation and cell alignment significantly impact melting rates and overall heat sink performance. These advancements highlight the critical role of TPMS structures in enhancing the thermal properties of PCMs, offering a versatile solution for next-generation cooling systems in high-performance electronics.

Although TPMS structures have shown potential for enhancing thermal management systems, the impact of lattice geometry, material selection, and PCM integration on heat sink performance under realistic operational conditions remains insufficiently explored. Most existing studies focus on isolated scenarios, lacking comprehensive evaluations across multiple design configurations and PCM types. This study aims to bridge this gap by systematically analysing four TPMS-based designs namely octahedral (P3), waveform (P2), droplet (P4) and primitive (P6) in combination with organic PCMs. By assessing their thermal performance under unidirectional heat flux, this research seeks to identify optimal design-PCM-material pairings for electronic cooling applications, addressing gaps in literature related to anisotropic heat dissipation, material compatibility, and design scalability. The novelty of this research lies in the design and analysis of compact TPMS-based metal lattice heat sinks using advanced additive manufacturing (AM) techniques. This study uniquely integrates three-dimensional numerical modelling with experimental validation to evaluate the performance of various TPMS configurations combined with phase change materials (PCMs). By systematically comparing metal lattice designs, this research investigates how geometric variations and material properties influence heat transfer and PCM melting dynamics.

While prior research has explored PCM integration in metal heat sinks using conventional geometries such as plate, cylindrical, or tree-shaped fins, very few studies have leveraged the unique surface properties of TPMS structures for enhanced thermal performance. Table 1 summarises key studies from the past five years, highlighting their core configurations and limitations. Notably, none of these works have compared multiple TPMS geometries or conducted experimental validation in conjunction with multi-PCM integration. Our study addresses this gap by conducting a comprehensive numerical and experimental analysis of four distinct TPMS lattice geometries embedded with three types of PCMs (RT31, RT42, and RT55), using both stainless steel and titanium fabricated via additive manufacturing.

2. Model

2.1. Designs

Four TPMS-based heat sink designs were developed to evaluate their thermal performance when integrated with phase change materials (PCMs) (Fig. 1). The four designs were named octahedral, waveform, droplet and primitive and were assigned P3, P2, P4 and P6, respectively. All designs share identical external dimensions of 15 mm × 15 mm × 32 mm to allow for a consistent comparison. Each heat sink was monolithic, featuring four mounting lugs at the base for securing onto a rig during experimental testing. P3, the main focus of this study, is characterized by a highly interconnected internal lattice structure designed to maximize thermal conductivity and heat dissipation efficiency. Designs P2, P4, and P6 feature unique geometric variations in their internal structures, aimed at enhancing different heat transfer mechanisms. A level set method was utilized to generate and optimize the TPMS geometries, while CAD modelling was performed using SolidWorks 2021. The designs were subsequently analyzed using ANSYS Fluent 2021 R2, where numerical simulations were conducted under consistent boundary conditions to assess thermal performance.

The design of experiments (DoE) involves a systematic evaluation of the heat sink designs under varying material and PCM configurations, as presented in Table 2. A total of 13 cases were analyzed, considering different combinations of heat sink designs (P3, P2, P4, and P6), materials (Stainless Steel (SS) and Titanium (Ti)), and PCMs (RT55, RT42, and RT31). The power input was maintained at a constant 8.6 W, with a heat transfer coefficient (HTC) of 40.0 W/m^{2}K, and ambient conditions set to atmospheric pressure. The P3 design was evaluated across

Table 1
Summary of recent PCM–heat sink studies (2020–2025).

Authors (year)	Geometry	Method	Boundary conditions	Material/PCM	Limitations/gap
Al-Omari et al. [2]	TPMS (gallium)	Numerical	High heat flux, natural convection	TPMS/Gallium	No multi-PCM; single geometry
Qureshi et al. [4]	TPMS	Experimental	Adiabatic walls	3D Printed + Organic PCM	No numerical model; limited geometry
Righetti et al. [5]	3D Printed Lattice	Experimental	Adiabatic, ambient	Paraffin	No thermal design variation
Qureshi et al. [6]	TPMS (porosity graded)	Numerical	Convection & conduction	TPMS/PCM	No experimental validation
Catchpole-Smith et al. [9]	TPMS Lattice	Experimental	Laser powder bed fusion	AlSi10Mg	No PCM integration
Qureshi et al. [11]	TPMS	Numerical	Symmetry + Natural convection	Organic PCM	No comparison with traditional fins
Sélô et al. [8]	Lattice	Experimental	Natural convection	AlSi10Mg	No PCM; focused on material manufacturing
Al-Omari et al. [24]	TPMS Fin	Numerical	Base heat flux, convective side	RT42	Single geometry and PCM
Al-Omari et al. [25]	TPMS Fin	Numerical	Parametric, base heating	RT55	No experimental support
Sampson et al. [31]	Porous grid (TPMS-like)	Numerical	Heat flux simulation	Metal foam	No PCM integration
Ali et al. [34]	Standard Heat Sink	Experimental	Ambient convection	RT42, RT50	No lattice geometry; conventional sink
Baig et al. [35]	Mini-channel	Numerical	Forced convection	Hybrid nanofluids	No PCM; no TPMS lattice
Present study	**TPMS (P2, P3, P4, P6)**	**Numerical + Experimental**	**Base heating + Convection on all other surfaces**	**SS/Ti with RT31/ RT42/RT55**	**Multi-PCM + Multi-geometry + Validation – Novel**

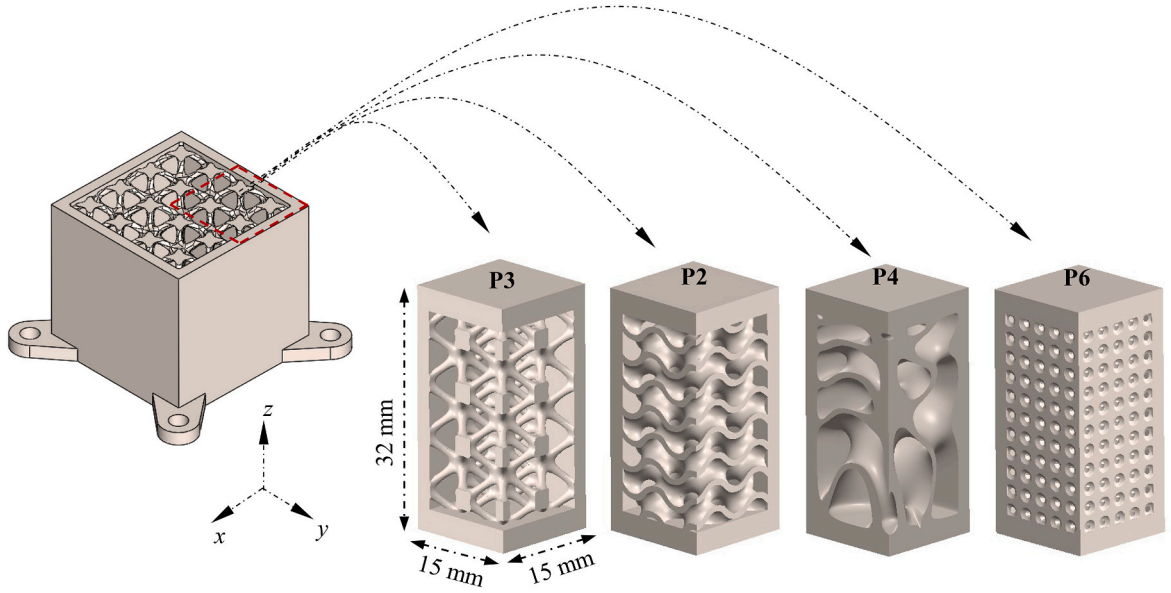

Fig. 1. CAD models of heat sink geometries, dimensions – all in mm.

Table 2
Design of experiments.

Cases	Design	Annotation	Material	Power input (W)	HTC (W/m^{2}K)	PCM	Ambient
1	Octahedral	P3	SS	8.6	40.0	RT55	Atmosphere
2	Octahedral	P3	Ti	8.6	40.0	RT55	Atmosphere
3	Octahedral	P3	SS	8.6	40.0	RT42	Atmosphere
4	Octahedral	P3	SS	8.6	40.0	RT31	Atmosphere
5	Waveform	P2	SS	8.6	40.0	RT55	Atmosphere
6	Waveform	P2	SS	8.6	40.0	RT42	Atmosphere
7	Waveform	P2	SS	8.6	40.0	RT31	Atmosphere
8	Droplet	P4	SS	8.6	40.0	RT55	Atmosphere
9	Droplet	P4	SS	8.6	40.0	RT42	Atmosphere
10	Droplet	P4	SS	8.6	40.0	RT31	Atmosphere
11	Primitive	P6	SS	8.6	40.0	RT55	Atmosphere
12	Primitive	P6	SS	8.6	40.0	RT42	Atmosphere
13	Primitive	P6	SS	8.6	40.0	RT31	Atmosphere

multiple PCM types and material variations, as it serves as the baseline for this study. For P2, P4, and P6 designs, Stainless Steel (SS) was used as the primary material, while the PCM was varied to assess its effect on heat transfer performance. The use of three PCM types (RT55, RT42, and RT31) allowed for comparison based on their thermophysical properties, such as melting temperature and latent heat storage capacity. This systematic approach ensures a comprehensive understanding of how lattice geometry, material selection, and PCM behaviour influence overall thermal performance.

2.1.1. Material

Two commonly used additive manufacturing materials, Stainless Steel 316L and Ti-6Al-4V, were selected for this study due to their contrasting thermophysical properties and widespread industrial applications. Stainless Steel 316L, with its higher thermal conductivity and lower specific heat, is better suited for heat transfer applications, as it enables rapid heat conduction from the PCM to the surrounding environment. In contrast, Ti-6Al-4V offers a lower density, making it ideal for lightweight applications, though it has relatively lower thermal conductivity compared to stainless steel. Both materials exhibit excellent corrosion resistance and high structural integrity, making them suitable for heat sink fabrication and integration with PCMs in latent heat energy storage systems. The manufacturing process for these designs was conducted using a Powder Bed Fusion Additive Manufacturing (PBF-AM) technique with a GE Concept Laser M2 Series 5 printer (400 W).

2.1.2. Internal structure

Each heat sink design integrates a distinct internal structure tailored for optimizing thermal performance and PCM melting dynamics. The P3 design features an intricate TPMS lattice structure, comprising 96 interconnected cells with a porosity of 85 % and an effective internal height of 26 mm. The smooth, continuous surface angles of the lattice were strategically chosen to enhance thermal exchange between the PCM and the heat sink walls. Design P2 incorporates wave-like TPMS patterns, which promote enhanced convection-driven heat transfer, particularly in liquid PCM regions. The P4 design, on the other hand, employs curved cellular structures, facilitating increased surface area contact for heat conduction while maintaining high porosity. Lastly, the P6 design consists of a perforated array of evenly spaced primitive voids, designed to optimize uniform thermal distribution and accommodate phase-change transitions efficiently. The diverse structural features of these designs enable a systematic comparison of heat transfer performance and thermal response across different geometric configurations.

2.1.3. Simulation domain

A quarter of each heat sink design was selected for numerical analysis due to its symmetrical properties. This approach reduces computational cost while maintaining the accuracy of the results. The simplified simulation domain included symmetry planes on two sides, a

uniform heat flux applied at the base, and convective boundary conditions applied on the remaining three sides to simulate natural convection. The full-sized heat sink model and its corresponding simplified numerical domain are illustrated in Fig. 1, and the associated design parameters are listed in Table 3. The mass values provided in Table 3 correspond only to the simplified quarter domain of the heat sinks. The total mass of the full heat sink can be estimated by multiplying these values by a factor of four to account for the symmetry and the remaining quarters. For instance, the total mass of design P3 (stainless steel) would approximate 30.68 g × 4 = 122.72 g. The same scaling applies to designs P2, P4, and P6, ensuring consistency between numerical and experimental analyses. It is important to note that minor deviations in the actual heat sink mass (P3) used for experiment may occur due to the inclusion of mounting lugs, feet, and small cavities incorporated to account for the expansion of the PCM upon melting. All four designs have lid on top correspond to the actual prints used in the experiments.

2.2. Numerical procedure

A 3D numerical model of the PCM-based metal lattice heat sink designs (P3, P2, P4, and P6) was generated and optimized using a level set method, as shown in Fig. 1. The heat sink models were analyzed under transient conditions to assess thermal performance with varying materials and PCMs at constant power input, as listed in Table 2. The simulations were performed using the pressure-based finite volume method (FVM) in ANSYS Fluent 2021 R2. For pressure-velocity coupling, the PRESTO scheme and PISO algorithm were employed to ensure numerical stability and convergence. A second-order upwind scheme was used for the convective terms to maintain solution accuracy, while a first-order implicit scheme was applied for time discretization in transient simulations. The under-relaxation factors were set at 0.3 for pressure, 0.7 for velocity, 1 for energy, and 0.9 for liquid fraction. Convergence criteria were defined with residuals set at 10^{-4} for continuity and momentum and 10^{-6} for the energy equation. The flow of liquid PCM within the cavity was assumed laminar, Newtonian, and incompressible, while the metal lattice remained solid, absorbing only sensible heat. The melting interface of the PCM was modelled using the mushy zone approach, with the Boussinesq approximation accounting for buoyancy-driven convection caused by density changes during phase transition. The thermophysical properties of Stainless Steel 316L, Titanium Ti-6Al-4V, and the selected PCMs (RT31, RT42, RT55) were assumed constant during the simulations, as detailed in Table 4. To simplify the analysis, volumetric expansion of the PCM during phase change and radiative heat transfer were neglected. Thermal resistance between the heater base and the heat sink was assumed negligible, ensuring direct thermal conduction from the heat source to the heat sink base.

2.3. Governing equations

The governing equations for the numerical analysis include the continuity, momentum, and energy equations, which describe the flow behaviour and thermal dynamics of the phase change material (PCM) and solid metal lattice structure. These equations account for buoyancy-driven convection, phase transition, and heat transfer mechanisms [4,6,11,26]:

Table 3
Stainless steel design parameters (quarter only).

Design	H (mm)	t_{base} (mm)	t_{lid} (mm)	t_{wall} (mm)	Mass (metal) (gram)	Mass (PCM) (gram)	Total Mass (gram)
P3	32	3	3	2	27.5	3.19	30.68
P2	32	3	3	2	33.8	2.62	36.42
P4	32	3	3	2	31.7	3.16	34.86
P6	32	3	3	2	35.6	2.41	38.01

Continuity equation:

$$\nabla.\mathbf{u} = 0 \tag{1}$$

Momentum equation:

$$\rho_f\left(\frac{\partial \mathbf{u}}{\partial t} + \mathbf{u}.\nabla\mathbf{u}\right) = -\nabla p + \mu_f\nabla^2\mathbf{u} + \rho_f g\beta\left(T_f - T_m\right) - \mathbf{S} \tag{2}$$

where $\mathbf{u}$ is the velocity vector (u, v, w), ρ_f is the fluid density, μ_f is the dynamic viscosity, $\nabla^2\mathbf{u}$ is the Laplacian of the velocity vector, p is the pressure, g is the gravitational acceleration, β is the thermal expansion coefficient and $\mathbf{S}$ is the source term vector $\left(S_x, S_y, S_z\right)$ expressed as:

$$\mathbf{S} = \frac{C(1-\lambda_l)^2}{\delta + {\lambda_l}^3} \tag{3}$$

where λ_l is the liquid fraction (ranging from 0 for solid to 1 for liquid), C is the mushy zone constant (set to 10^5) and $\delta = 0.001$ is a small constant to avoid singularities near zero liquid fraction [27,30].

The energy equation governs the heat transfer and phase change process within the PCM:

$$\rho_f C_{p,f}\left(\frac{\partial T_f}{\partial t} + \mathbf{u}.\nabla T_f\right) = k_f\nabla^2 T_f - \rho_f L\,\frac{\partial \lambda_l}{\partial t} \tag{4}$$

The liquid fraction λ_l is temperature-dependent and updated as follows:

$$\lambda_l = \begin{cases} 0, & if\ T_f \le T_{sol} \\ \dfrac{T_f - T_{sol}}{T_{liq} - T_{sol}}, & if\ T_{sol} \le T_f \le T_{liq} \\ 1, & if\ T_f \ge T_{liq} \end{cases} \tag{5}$$

where $C_{p,f}$ is the specific heat and k_f is the thermal conductivity of the PCM. L is the latent heat of fusion T_{sol} and T_{liq} are the solidus and liquidus temperatures of the PCM, respectively. For the solid metal lattice structure, where no phase change occurs, the energy equation simplifies to unsteady heat conduction:

$$\rho_s C_{p,s}\left(\frac{\partial T_s}{\partial t}\right) = k_s\nabla^2 T_s \tag{6}$$

where ρ_s is the density, $C_{p,s}$ is the specific heat and k_s is the thermal conductivity of the solid material.

2.4. Initial and boundary conditions

The initial and boundary conditions applied in the simulations are illustrated in Fig. 2. To replicate realistic operating conditions, convection boundary conditions were applied to the outside walls and the top surface of the heat sink lid. The heat transfer coefficient (HTC) was set to 40 W/m^{2}K to mimic natural convective heat dissipation into the surrounding air at room conditions. A uniform heat-flux boundary condition was imposed at the base of the heat sink to simulate the heat generated by the heater chip. The heat dissipation was measured to be approximately 8.6 W, corresponding to the heater's maximum operational capacity. This power value was uniformly distributed over the bottom wall surface area to compute the applied heat flux. The initial temperature of the heat sink and the phase change material (PCM) was set to 24.5 °C for all cases, representing the ambient room temperature. Additionally, the initial velocity was assumed to be zero ($V_{ini} = 0$ m/s), as the PCM was initially in a solid state.

2.5. Grid independence and time step sensitivity analysis

The computational grid used in the simulations is illustrated in Fig. 2 (b). To optimize computational efficiency, non-critical features such as

Table 4
Thermo-physical properties of materials included in the analysis [36–38].

Materials	Properties							
	Density $\left(\frac{kg}{m^3}\right)$	Specific heat $\left(\frac{J}{kgK}\right)$	Thermal conductivity $\left(\frac{W}{mK}\right)$	Viscosity $(\frac{kg}{m.s})$	Thermal expansion coefficient, β $\left(\frac{1}{K}\right)$	Latent heat, L $(\frac{kJ}{kg})$	Solidus temperature (°C)	Liquidus temperature (°C)
Titanium (Ti-6Al-4V)	4850	544.25	11.4	–	–	–	–	–
Stainless steel (316L)	8030	502	16.2	–	–	–	–	–
RT31	880	2000	0.2	0.0251	0.00011	165	27	33
RT42	880	2000	0.2	0.0235	0.0001	165	38	43
Wax (~RT55)	880	2000	0.2	0.03	0.00011	170	53	58

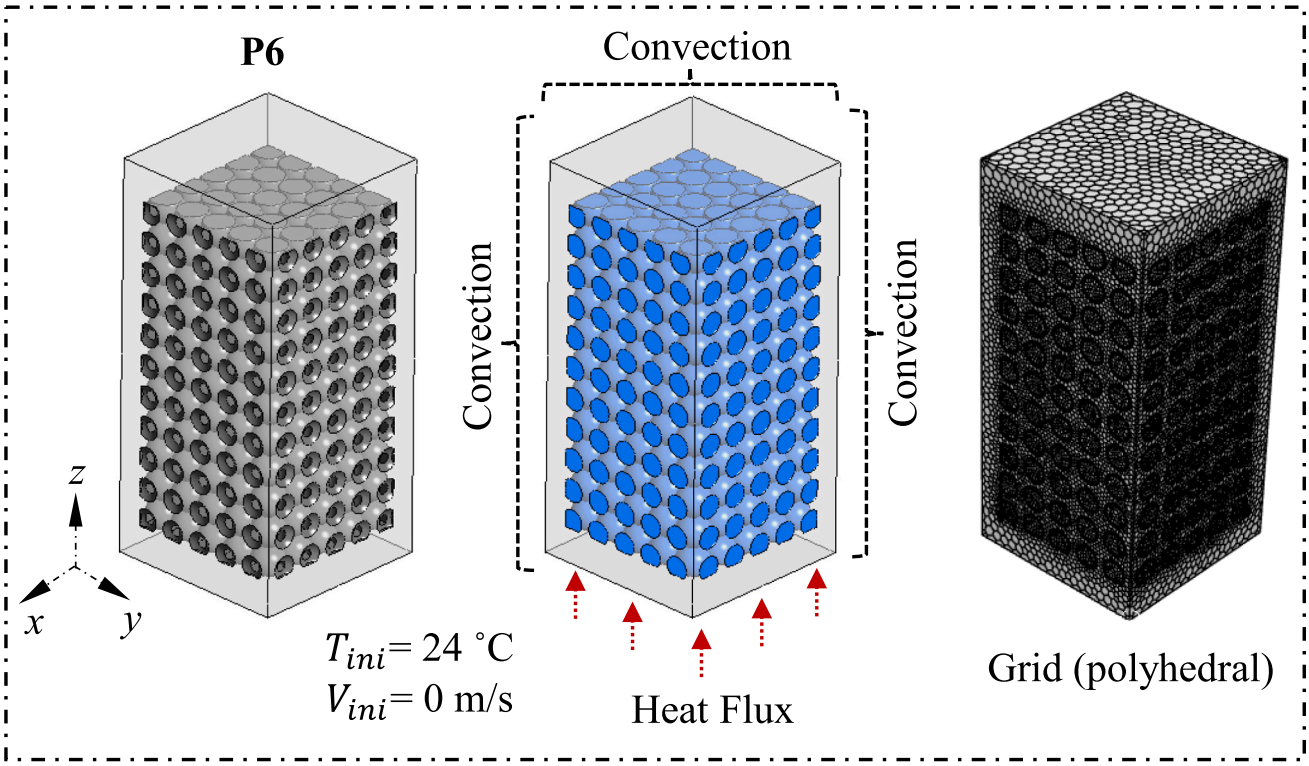

Fig. 2. Example of (a) Initial and boundary conditions; (b) computational grid.

mounting lugs, fillets, holes, and rounded corners were removed prior to meshing. An initial tetrahedral/hexahedral mesh was converted into a polyhedral mesh, reducing the total cell count while maintaining simulation accuracy. The mesh quality was validated, with over 99 % of cells showing an orthogonal quality above 0.8. Only 1 % of cells were below this threshold, ensuring the grid's suitability for simulations. Grid independence analysis was performed to evaluate the effect of mesh resolution on simulation accuracy. Five grid systems, ranging from 478 K to 6.9 M cells, were tested, as summarized in Table 5. The melting time and base temperature were compared for all grid sizes, showing deviations of <0.08 % and 0.1 %, respectively. As shown in Fig. 3 (a), the liquid fraction profiles exhibit negligible variation across different grid sizes, confirming grid independence. Grid 3 (2.1 M cells) was selected for all subsequent simulations, as it provided an optimal balance between computational accuracy and time efficiency. Time step sensitivity analysis was conducted using four time steps: 1.5 s, 1.0 s, 0.5 s, and 0.1 s. The results, illustrated in Fig. 3 (b), indicate that the maximum variation in liquid fraction and temperature across time steps was <0.2 % at equal physical times. A time step of 0.5 s was deemed sufficient to achieve time-independent results while minimizing computational effort. This configuration ensured accurate and reliable predictions of the phase change dynamics within the heat sink.

Table 5
Summary of grid independence analysis (P3 only).

Grid system	No. of cell	Melting time (s)	Deviation (%)	Base temp (°C)	Deviation (%)
G-1	478 K	3472	0.00	91.17	0.00
G-2	1.3 M	3476	0.08	91.07	0.10
G-3	2.1 M	3479	0.03	91.02	0.05
G-4	3.6 M	3481	0.02	90.97	0.05
G-5	6.9 M	3484	0.03	90.92	0.05

3. Experiment

3.1. Setup and procedure

The experimental setup consisted of a heat sink mounted onto a custom-designed printed circuit board (PCB) equipped with an electric heater and a thermistor placed at the centre of the heater. As illustrated in Fig. 4 (a), the thermistor was centrally positioned within the heated area to monitor the base temperature of the heat sink at 5-s intervals. A

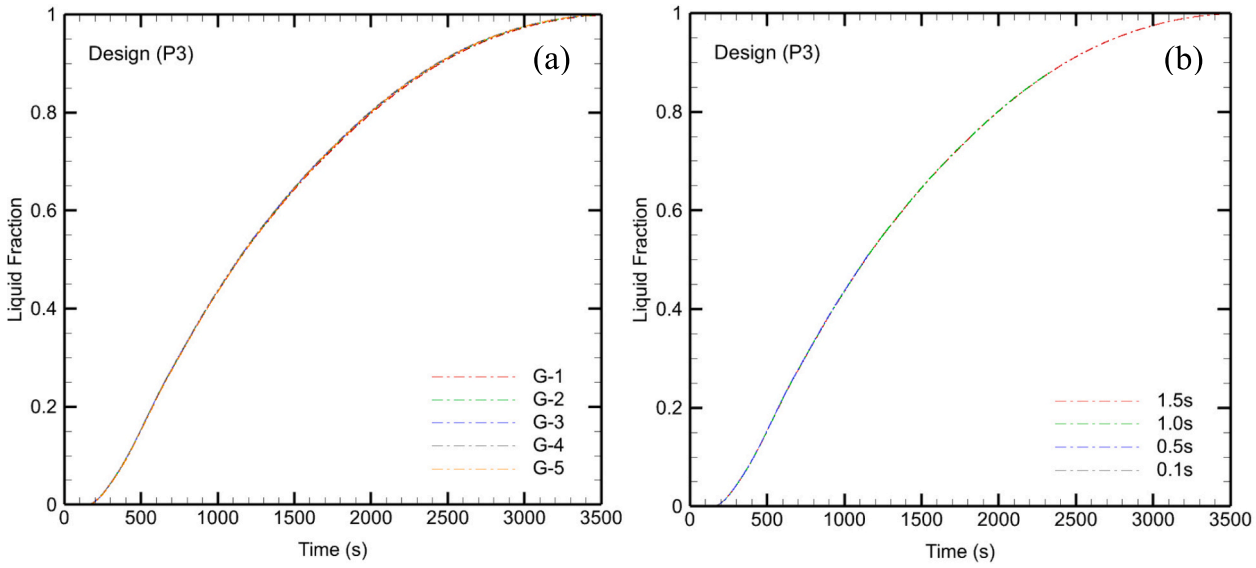

Fig. 3. Stainless steel design P3 liquid fraction (a) grid independence; (b) time step sensitivity.

BeagleBone Black microprocessor was used to process the temperature data, which was then transmitted wirelessly to a web-based control dashboard. The system was powered by a battery. Fig. 4 (b) shows a photograph of the actual PCB board with the attached heat sink, battery, microprocessor, and wiring setup, while Fig. 4 (c) displays the printed TPMS-based heat sink designs fabricated using additive manufacturing. The heat sink absorbed heat generated by the electric heater and transferred it to the phase change material for thermal energy storage. Paraffin wax (Sigma-Aldrich 327204) was selected as the PCM due to its uniform melting behaviour, chemical stability, and minimal volumetric expansion during phase change. The wax (analogous to RT55) has a melting temperature range of 53 to 58 °C and a mass of 6 g, occupying approximately half of the heat sink's internal volume when in liquid form. To ensure consistent thermal performance, Apiezon H thermal grease was applied between the heater and the heat sink base to minimize thermal contact resistance.

For the experimental tests, the heater area on the PCB was 30 × 30 mm^2, and it operated at a constant power of 8.6 W throughout all tests. The heater power was determined using measured resistance (2.3 Ω) and voltage (4.46 V) values at ambient temperature, with uncertainties of ±1.5 % for resistance and ± 0.5 % for voltage. Tests were conducted under standard laboratory conditions at room temperature and atmospheric pressure, without any additional enclosures or isolation. Two variations of the experiments were performed using the P3 heat sink design fabricated from Titanium (Ti-6Al-4V) and Stainless Steel (316L), as summarized in Table 6. Each test was repeated three times to ensure repeatability and consistency. The heat sink was mounted on the PCB using nylon screws to prevent additional heat loss through conduction.

During each test, the initial temperature of the setup was maintained at 23 °C ± 1.5 °C, with the heater turned off. Once the heater was switched on, the thermistor recorded the temperature at the heat sink base at 5-second intervals. Following this, the heater was turned off.

4. Results and discussion

4.1. Validation

Fig. 5 illustrates the experimental validation of the base temperature profiles for the P3 heat sink design made from Titanium (Ti) and Stainless Steel (SS), subjected to a constant heater power input of 8.6 W. The results show an initial steady rise in temperature for both materials due to the dominance of conduction heat transfer in the pre-sensible heating phase, where the heat is primarily absorbed by the metal structure. The titanium heat sink reached a maximum base temperature of approximately 98 °C in an hour, while the stainless-steel heat sink stabilized at a lower base temperature of about 90 °C during the same period. This discrepancy can be attributed to the lower thermal conductivity of titanium compared to stainless steel, as stainless-steel conducts approximately 1.4 times more heat than titanium. Consequently, the temperature rise in the stainless-steel heat sink was slower and more uniform, whereas titanium exhibited a sharper temperature increase.

The experimental results closely align with the numerical simulations, as shown by the overlapping trends in Fig. 5. The maximum temperature difference between the experimental and simulation results was 3.7 °C for stainless steel and <2 °C for titanium. These minor deviations can be linked to factors such as variations in the realized thermal conductivity of the additively manufactured heat sinks, the presence of air gaps at the PCM interface during the experiments, and the exclusion of PCM volume expansion effects in the simulation model. Despite these differences, the temperature profiles in both cases remain smooth and stable, with a noticeable flattening of the curve during the phase transition period of the PCM. This behaviour highlights the PCM's ability to absorb heat as latent heat, effectively stabilizing the temperature rise and providing a thermal buffer.

The titanium heat sink, due to its lower thermal conductivity, demonstrated a less efficient heat-spreading capability, resulting in a faster temperature rise. However, the integration of PCM mitigated this effect by maintaining a stable and lower base temperature during operation. The PCM's high specific heat capacity (2000 J/kg·K) allowed it to absorb substantial amounts of heat, extending the operational duration of the heat sink while keeping temperatures within acceptable limits. The numerical simulations further confirm these findings, showing similar thermal behaviour, albeit with a longer phase transition period. This is attributed to the absence of PCM volume expansion in the simulations, which in experiments perturbed the flow dynamics, leading to localized variations in temperature profiles. The lower base temperature observed in stainless steel is attributed to its higher thermal conductivity (16.2 W/m·K) compared to titanium (11.4 W/m·K), which enables more effective conduction of heat away from the source. Additionally, the phase transition plateau seen in the temperature profile reflects the absorption of latent heat by the PCM, which buffers temperature rise. This behaviour confirms that both material selection and latent heat absorption significantly influence thermal regulation during operation.

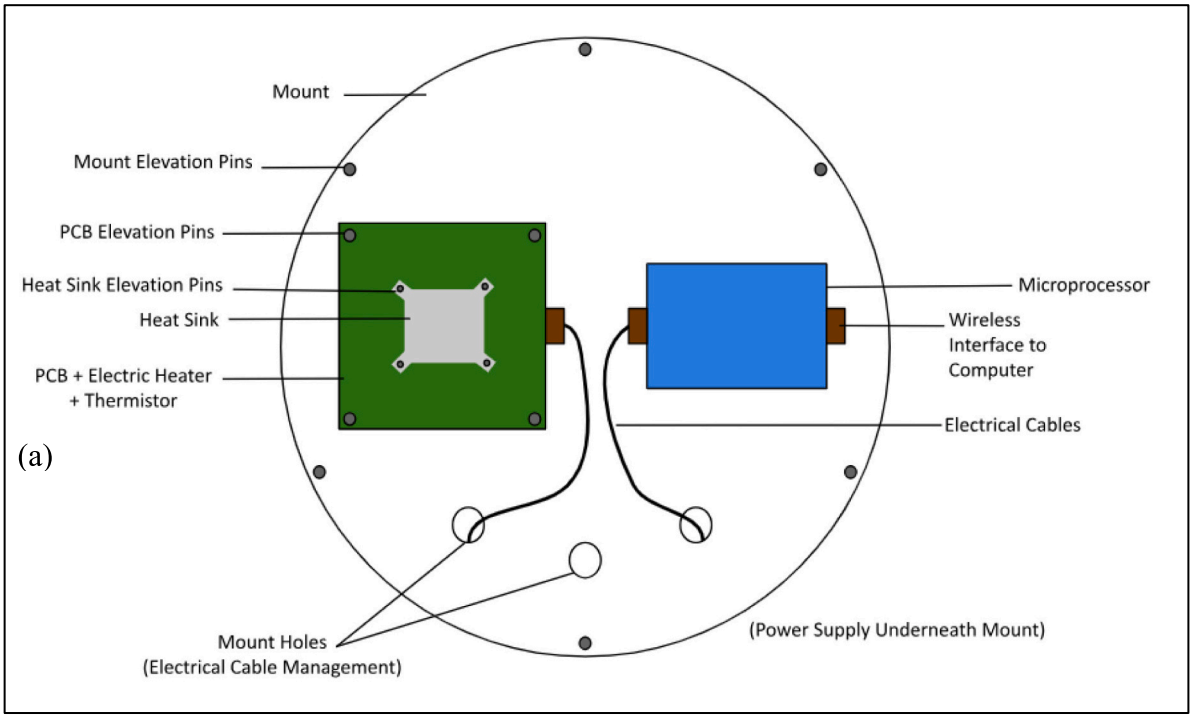

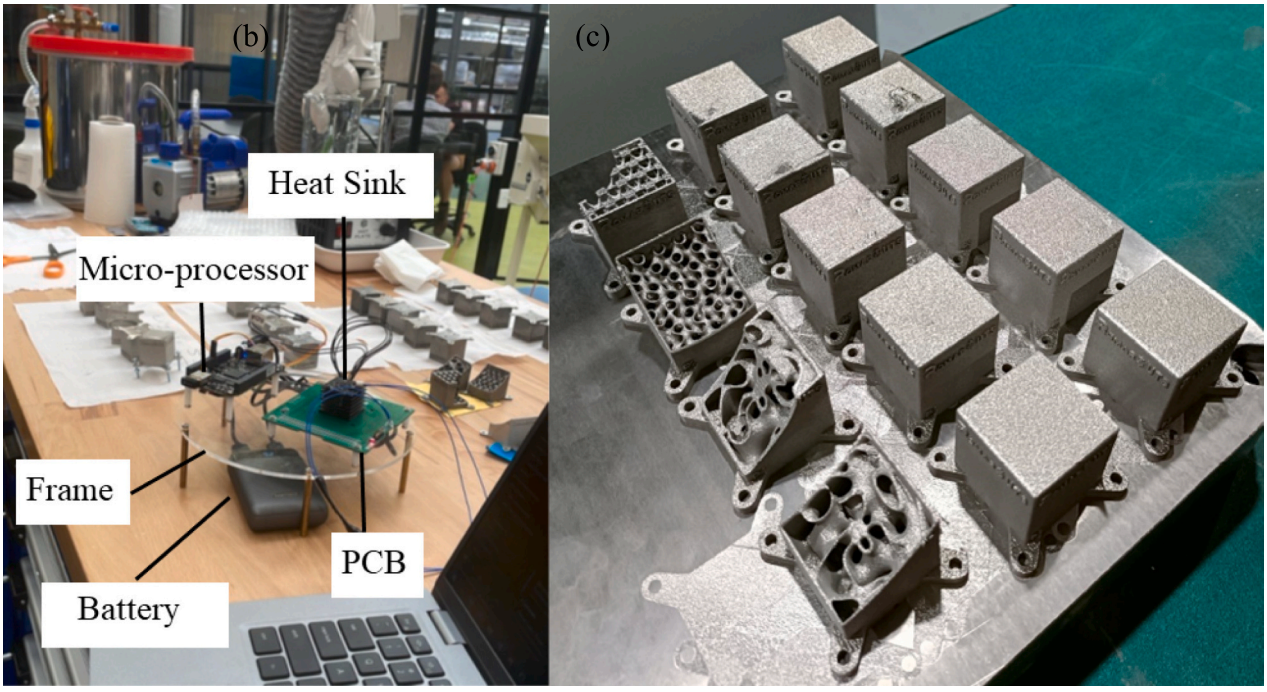

Fig. 4. Experimental set-up (a) 2-D schematic showing test setup with mounting arrangements; (b) picture depicting actual PCB board, battery, sensors and a microprocessor; (c) actual prints of designs.

Table 6
Variation of experimental tests.

Test Variation	Material	PCM Mass (g)	Heater power (W)	Ambient
Design (P3)	Titanium (Ti-6Al-4V)	6	8.6	Atmosphere
Design (P3)	Stainless Steel (316L)	6	8.6	Atmosphere

The validation results demonstrate the effectiveness of integrating PCM with the TPMS-based metal lattice heat sink. Stainless steel outperformed titanium by maintaining lower base temperatures, attributed to its superior thermal conductivity. The combination of PCM with the lattice structure ensured smooth and stable temperature rise, highlighting its effectiveness as a thermal energy storage system. The close agreement between the experimental and numerical results highlights the reliability of the simulation model in predicting the thermal behaviour of the heat sink, confirming its suitability for advanced thermal management applications.

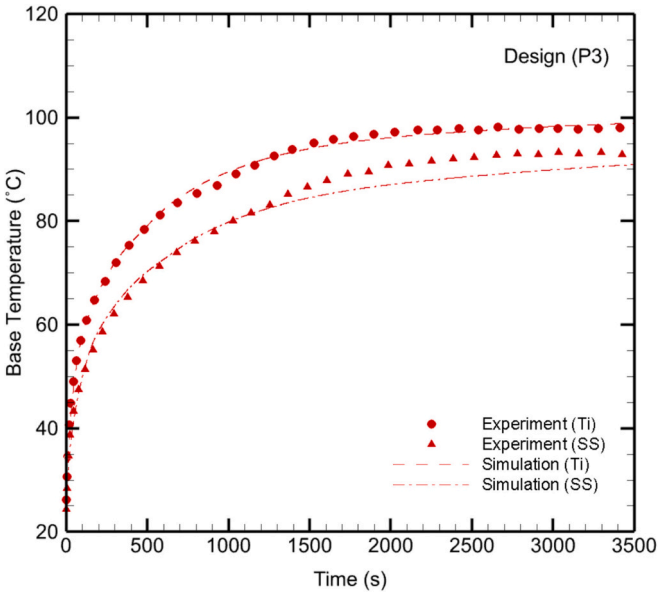

Fig. 5. Experimental validation for design P3 (titanium and stainless steel).

4.2. Contours of liquid fraction and temperature

The inclusion of the TPMS-based metal lattice structure within the cavity, combined with the boundary conditions and thermal mass of the designs, significantly influences the PCM flow dynamics and heat transfer processes, as depicted in Figs. 6 (liquid fraction) and 7 (temperature). Initially, the PCM remains in its solid state because the supplied heat is absorbed by the metal lattice structure, increasing its temperature until the PCM melting point is reached. Heat transfer begins through conduction at the lattice-PCM interface, where the thermal mass of the designs and their respective internal structures dictate the rate of heat propagation and melting progression.

In the early stages of melting (500–1500 s), P6 demonstrates the fastest melting progression due to its symmetrical lattice structure, which promotes uniform heat transfer and minimizes thermal resistance. The symmetrical design of P6 allows for efficient convective flow patterns, leading to rapid heat penetration through the PCM volume. Design P2, with its smooth and continuous lattice walls, follows closely, facilitating effective upward heat transfer. Meanwhile, P3 exhibits moderate melting progression, aided by its lightweight and optimized porosity. In contrast, P4 shows the slowest melting due to its complex internal lattice structure, which restricts convective flow dynamics and increases localized thermal resistance. This can be physically explained by the complexity of P4's internal pathways, which increases conduction path lengths and restricts buoyancy-driven flow. As melting proceeds, the onset of natural convection is governed by thermal gradients, and the design's ability to support vertical convection cells becomes critical. Designs such as P6 with symmetrical and vertically connected lattice paths promote the formation of Bernard convection cells, leading to more uniform and faster PCM melting. As melting progresses (2000–3000 s), natural convection becomes dominant, as evidenced by the formation of Bernard convection cells near the lattice-PCM interface. These convection cells promote upward heat transfer, accelerating the melting front toward the top of the heat sink. The contours in Fig. 6 show that designs P6 and P2 maintain a more uniform and rapid progression of the liquid fraction due to their efficient flow paths and symmetrical geometries. The P3 design follows, benefitting from its lightweight and porosity, while P4 continues to exhibit slower melting due to the constrained flow patterns created by its internal lattice geometry.

The temperature contours in Fig. 7 further emphasize the thermal behaviour of the different designs. At the early stages (500–1500 s), temperature stratification is clearly observed, with higher temperatures concentrated near the base where heat is applied. As time progresses (2000–3500 s), the thermal distribution becomes more uniform, driven by the combined effects of conduction through the lattice and natural convection within the PCM. The P6 design remains the coolest throughout the process, followed closely by P2. Both designs benefit from their higher thermal masses, which facilitate efficient heat

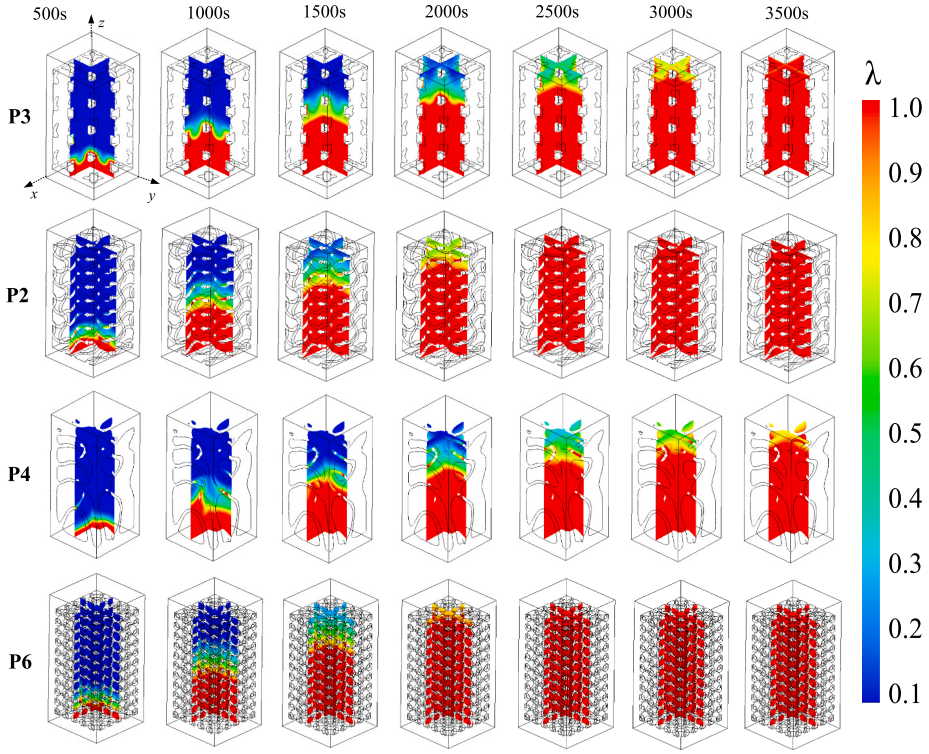

Fig. 6. Transient contours of liquid fraction at full heater power (stainless steel).

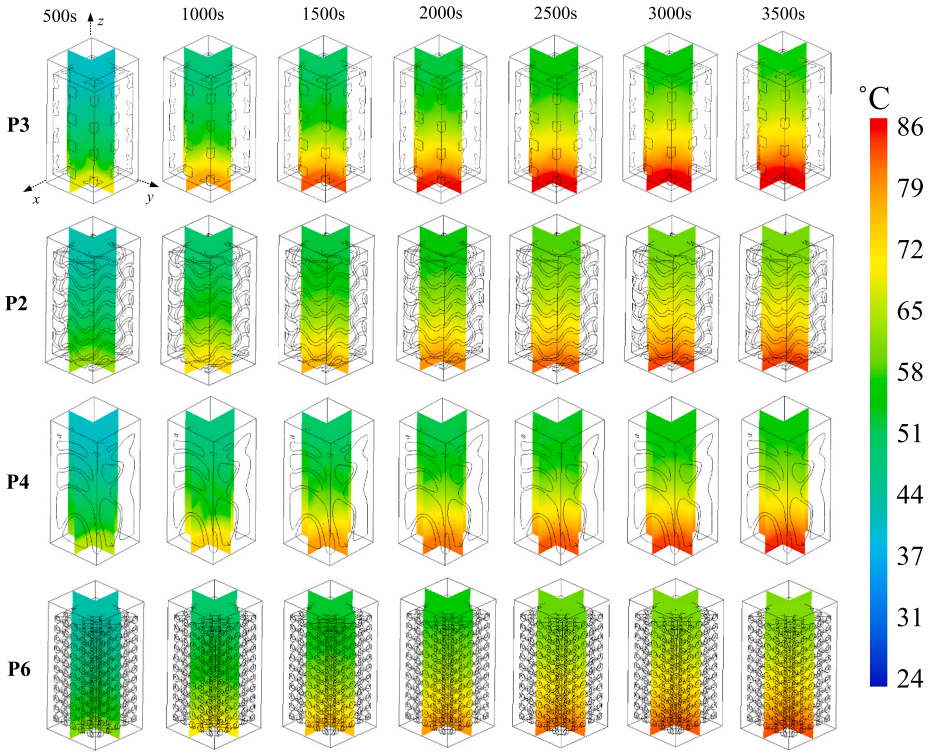

Fig. 7. Transient contours of temperature at full heater power (stainless steel).

dissipation and prevent localized overheating. On the other hand, P3 exhibits the highest temperatures due to its lower thermal mass and lightweight structure, which reduce heat exchange between the metal lattice and PCM. Design P4 follows closely, as its complex internal structure impedes heat transfer efficiency, resulting in localized temperature gradients and slower heat dissipation. These observations highlight the role of thermal mass and internal lattice geometry in determining the heat sink's thermal performance under full heater power.

Among all the designs, P6 emerges as the best-performing design in terms of heat transfer capabilities, demonstrating the fastest melting and lowest base temperatures due to its symmetrical lattice structure and optimized thermal mass. However, P3, despite being the hottest, excels in terms of energy storage for prolonged operation. Its lightweight and high porosity enable it to absorb significant amounts of thermal energy while maintaining temperatures well below critical operating limits for extended durations. These results demonstrate a balance between heat transfer efficiency and thermal energy storage, where P6 is ideal for rapid heat dissipation, while P3 offers longer thermal management capabilities. From a heat transfer perspective, the superior performance of P6 arises from reduced thermal resistance, high surface area-to-volume ratio, and balanced distribution of heated surfaces. In contrast, P4's uneven lattice arrangement introduces local stagnation zones, hindering convective transport and delaying melting.

4.3. Effect of PCMs

4.3.1. Base temperature profiles

The performance of the TPMS-based heat sink designs (P3, P2, P4, and P6) was evaluated using three different PCMs: RT55, RT42, and RT31. The transient base temperature profiles, as shown in Fig. 8(a), (b), and (c), reveal the influence of PCM thermal properties, such as melting temperature and latent heat capacity, as well as the heat sink lattice structure on thermal performance. In the initial heating stage (up to approximately 500 s), a rapid temperature rise occurs for all designs and PCMs due to conduction-dominated heat transfer through the metal lattice to the PCM. This phase precedes the onset of phase change, where the heat is primarily absorbed by the metal before being transferred to the PCM. Beyond this point, the melting temperature of the PCM and the lattice structure determine the thermal behaviour.

For RT55 (Fig. 8 (a)), P6 consistently achieves the lowest base temperature throughout the duration, stabilizing at approximately 82 °C after 3500 s. This is attributed to its symmetrical lattice structure, which enhances heat transfer and accelerates PCM melting. P2, with its smooth lattice structure and higher thermal mass, follows closely with a base temperature of 84 °C. In comparison, P3 and P4 exhibit higher base temperatures of 88 °C and 90 °C, respectively. The lightweight structure of P3 accelerates the temperature rise, while P4's complex lattice geometry restricts efficient heat propagation and PCM interaction. With RT42 (Fig. 8 (b)), the earlier onset of phase change enhances the thermal buffering effect, reducing base temperatures more effectively. P6 again demonstrates superior performance, stabilizing at 78 °C by 3500 s. P2 maintains a slightly elevated base temperature of 80 °C, while P3 and P4 reach 85 °C and 87 °C, respectively. The quicker activation of RT42 improves convective heat transfer at the lattice-PCM interface, particularly benefiting P6 and P2 due to their uniform heat transfer pathways. For RT31 (Fig. 8 (c)), the lower melting temperature enables earlier phase change and provides extended thermal buffering. This results in the most significant reduction in base temperature. P6 stabilizes at approximately 72 °C, highlighting its ability to facilitate rapid melting and efficient thermal control. P2, with a similar structure, achieves a base temperature of 75 °C. In contrast, P3 and P4 exhibit slightly higher base temperatures of 78 °C and 80 °C, respectively. The earlier phase change initiation in RT31 delays the temperature rise and improves heat dissipation across all designs. The phase transition onset in each PCM depends on its melting temperature and latent heat. RT31 begins melting earlier, which means that it starts absorbing latent heat sooner, flattening the temperature profile and delaying further rise. This latent heat buffering explains why all designs show lower temperatures with RT31. The sharper temperature rise in RT55 is due to the higher energy required to reach its phase change threshold, and its delay in initiating latent heat absorption.

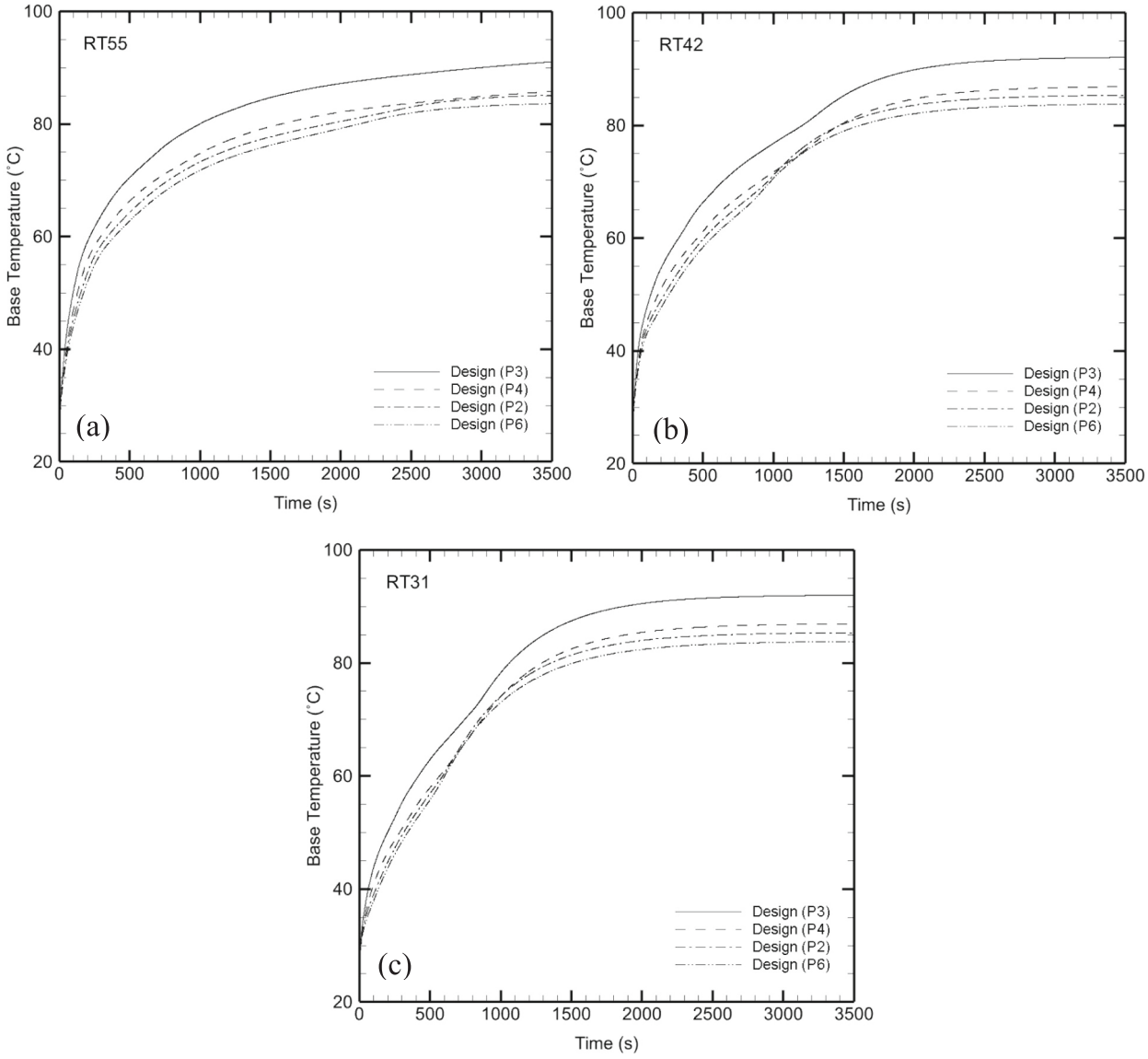

Fig. 8. Base temperature profiles for (a) RT55; (b) RT42; and (c) RT31.

The summarized times to reach critical base temperatures (Tcr = 50 °C, 60 °C, 70 °C, and 80 °C) for all PCM-heat sink combinations are presented in Table 7. The base temperature profiles indicate that P3 reaches critical temperatures the fastest across all PCMs due to its lightweight structure, which promotes rapid heat absorption and temperature rise, while P4 consistently takes the longest time, attributed to its complex internal geometry that restricts heat transfer efficiency. The lightweight and porous nature of P3 means it has lower thermal inertia and reduced heat-spreading capacity. Consequently, less energy is diverted to lattice preheating, and more is rapidly transferred to the PCM near the heat source, accelerating the base temperature rise.

Table 7
Time (s) to reach critical base temperatures.

Design	PCM type	T_{cr} = 50 °C	T_{cr} = 60 °C	T_{cr} = 70 °C	T_{cr} = 80 °C
P3	RT55	99	218	482	1000
P3	RT42	131	328	640	1207
P3	RT31	200	419	746	1062
P4	RT55	130	294	682	1578
P4	RT42	182	460	902	1471
P4	RT31	285	569	869	1294
P2	RT55	153	343	776	1913
P2	RT42	227	509	958	902
P2	RT31	314	590	850	1358
P6	RT55	174	393	871	2135
P6	RT42	259	562	979	1619
P6	RT31	342	604	879	1517

4.3.2. *Average temperature profiles*

The average temperature profiles for the heat sink designs (P3, P4, P2, and P6) using PCMs RT55, RT42, and RT31 are shown in Fig. 9 (a), (b), and (c). These profiles represent the combined average temperature of the metal and PCM, revealing the influence of PCM thermal properties, phase change onset, and the internal heat sink geometry on thermal performance. During the initial heating phase (up to approximately 500 s), the temperature rise is predominantly driven by conduction heat transfer through the metal lattice structure. At this stage, designs with simpler and more symmetrical geometries, such as P6 and P2, demonstrate a faster temperature response due to efficient thermal pathways and higher thermal mass. Conversely, P4, with its complex lattice structure, exhibits delayed thermal propagation as localized stagnation zones restrict uniform conduction and heat transfer. P3, being lightweight and porous, rises steeply in temperature due to its lower thermal

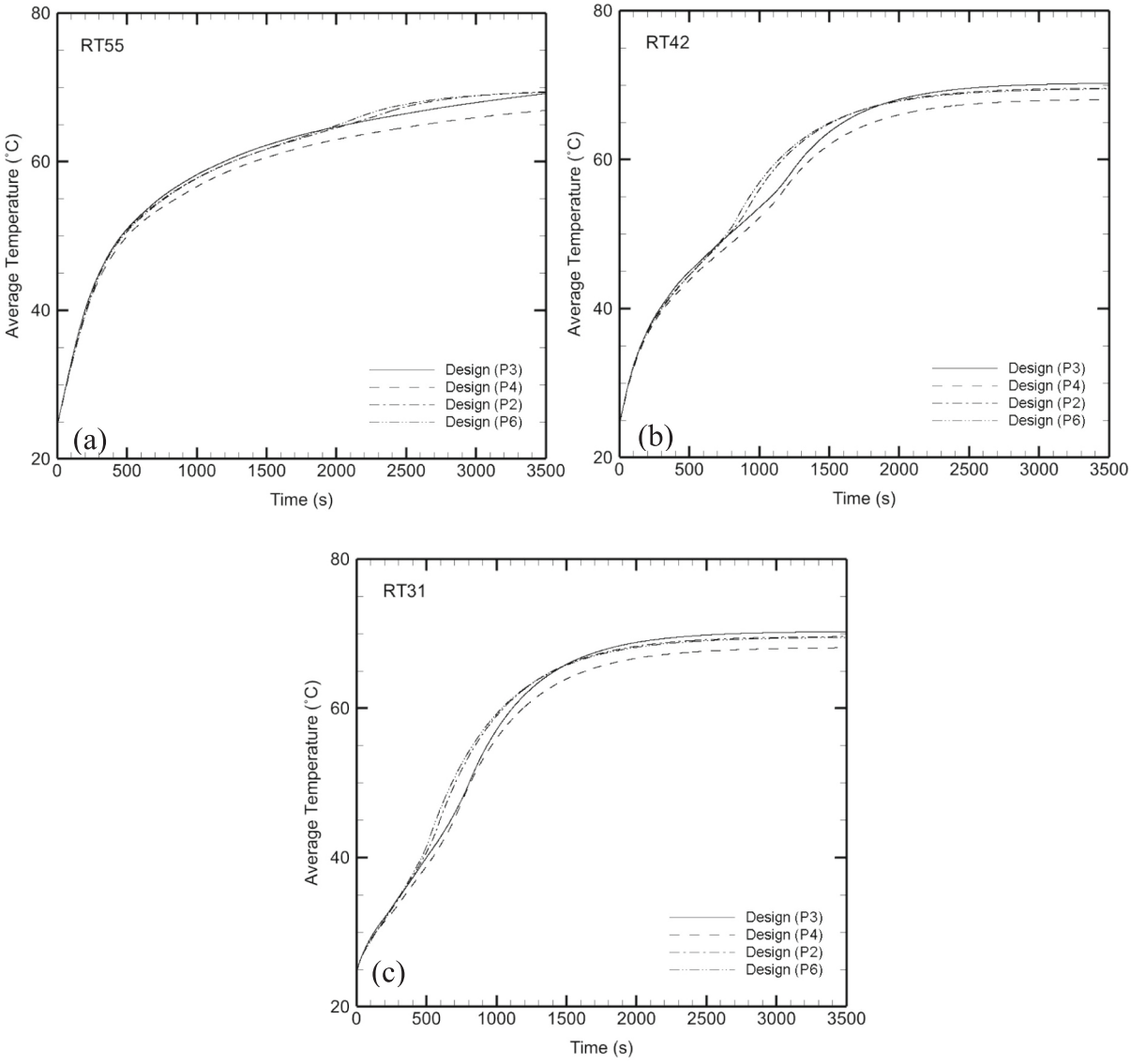

Fig. 9. Average temperature profiles for (a) RT55; (b) RT42; and (c) RT31.

mass and reduced heat exchange efficiency. The phase change process begins earlier for RT31 due to its lower melting temperature (31 °C) compared to RT42 (42 °C) and RT55 (55 °C). This earlier phase change onset for RT31 enables better thermal buffering, moderating the temperature rise across all designs. For instance, with RT31, the average temperature in P6 stabilizes at approximately 52–54 °C much earlier compared to P3 and P4. In contrast, RT55, with its higher melting point, delays the onset of phase change, leading to a steeper temperature rise before stabilization. These average profiles reflect combined conductive and convective contributions. While conduction dominates in early stages, natural convection in melted regions redistributes heat vertically. The designs with streamlined flow paths (P6 and P2) enhance vertical convective currents, reducing thermal stratification and enabling more uniform heat distribution.

The influence of the lattice geometry is also significant during the melting process. P6, with its symmetrical and evenly distributed lattice structure, achieves consistent and uniform heat transfer, resulting in the fastest stabilization of average temperatures. In contrast, P4's irregular lattice geometry restricts convective flow and prolongs heat transfer, causing higher average temperatures over time. For example, with RT55, P4 reaches 60 °C in 504 s, compared to 474 s for P6 (Table 8). P3, despite its rapid temperature rise, offers advantages in thermal energy storage due to its lightweight structure. Although it consistently reaches higher average temperatures sooner, this design is favourable for prolonged energy storage applications requiring extended operation at lower power levels. P2 performs similarly to P6 but with slightly slower heat dissipation due to its higher thermal mass, which delays temperature stabilization. The earlier stabilization in P6, particularly with RT31,

Table 8
Time (s) to reach critical average temperatures.

Design	PCM Type	$T_{cr} = 40$ °C	$T_{cr} = 50$ °C	$T_{cr} = 60$ °C	$T_{cr} = 70$ °C
P3	RT55	200	459	1196	–
P3	RT42	291	788	1299	2885
P3	RT31	501	806	1114	2721
P4	RT55	214	504	1409	–
P4	RT42	318	875	1368	–
P4	RT31	545	814	1191	–
P2	RT55	208	465	1253	–
P2	RT42	300	784	1169	–
P2	RT31	481	706	1050	–
P6	RT55	214	474	1254	–
P6	RT42	305	767	1140	–
P6	RT31	465	682	1039	–

reflects efficient coupling between lattice structure and phase change thermodynamics. High porosity and uniform geometry facilitate thermal exchange, while early-melting PCMs like RT31 start utilising latent heat earlier. This synergy is less prominent in P4, where irregular lattice channels inhibit convective mixing and prolong temperature rise. The summarized time to reach critical average temperatures (Tcr = 40 °C, 50 °C, 60 °C, and 70 °C) for all PCM-heat sink combinations is presented in Table 8. The table highlights that P6 achieves the fastest stabilization across all critical temperatures and PCMs, with RT31 performing the best due to its lower melting point.

4.3.3. *Liquid fraction*

The liquid fraction profiles for the PCM-heat sink combinations, as shown in Fig. 10 (a), (b), and (c), illustrate the melting progression of RT55, RT42, and RT31 in designs P3, P4, P2, and P6. These profiles provide a comprehensive understanding of the influence of PCM melting temperature and the internal lattice structure on the phase change process. In the early heating stages (0–500 s), the melting process is dominated by conduction heat transfer from the heat sink base through the lattice to the PCM. Designs P6 and P2 show a faster onset of melting due to their symmetrical and continuous lattice geometries, which enhance uniform heat distribution. By contrast, P4 experiences delayed melting because its complex internal lattice creates localized thermal resistances, slowing heat propagation. P3, though lightweight and porous, also exhibits slower melting compared to P6 and P2 due to reduced thermal mass and limited heat transfer efficiency.

For RT55 (Fig. 10 (a)), which has the highest melting point (55 °C), the melting process is notably slower. Complete melting for RT55 occurs at approximately 3214 s in P3, whereas P6 achieves full melting the fastest at 2009 s, followed closely by P2 at 2192 s (Table 9). P4, on the other hand, lags significantly, taking 3592 s due to its thermal resistance. In the case of RT42 (Fig. 10 (b)), the lower melting point (42 °C) accelerates the phase change process. P6 reaches complete melting in 802 s, outperforming all other designs due to its efficient heat transfer pathways and thermal symmetry. P2 follows closely, achieving full melting at 875 s. Designs P4 and P3 again show slower progression, with P4 taking 1113 s and P3 requiring 1156 s to achieve full melting. The melting process is fastest for RT31 (Fig. 10 (c)), with its melting point at

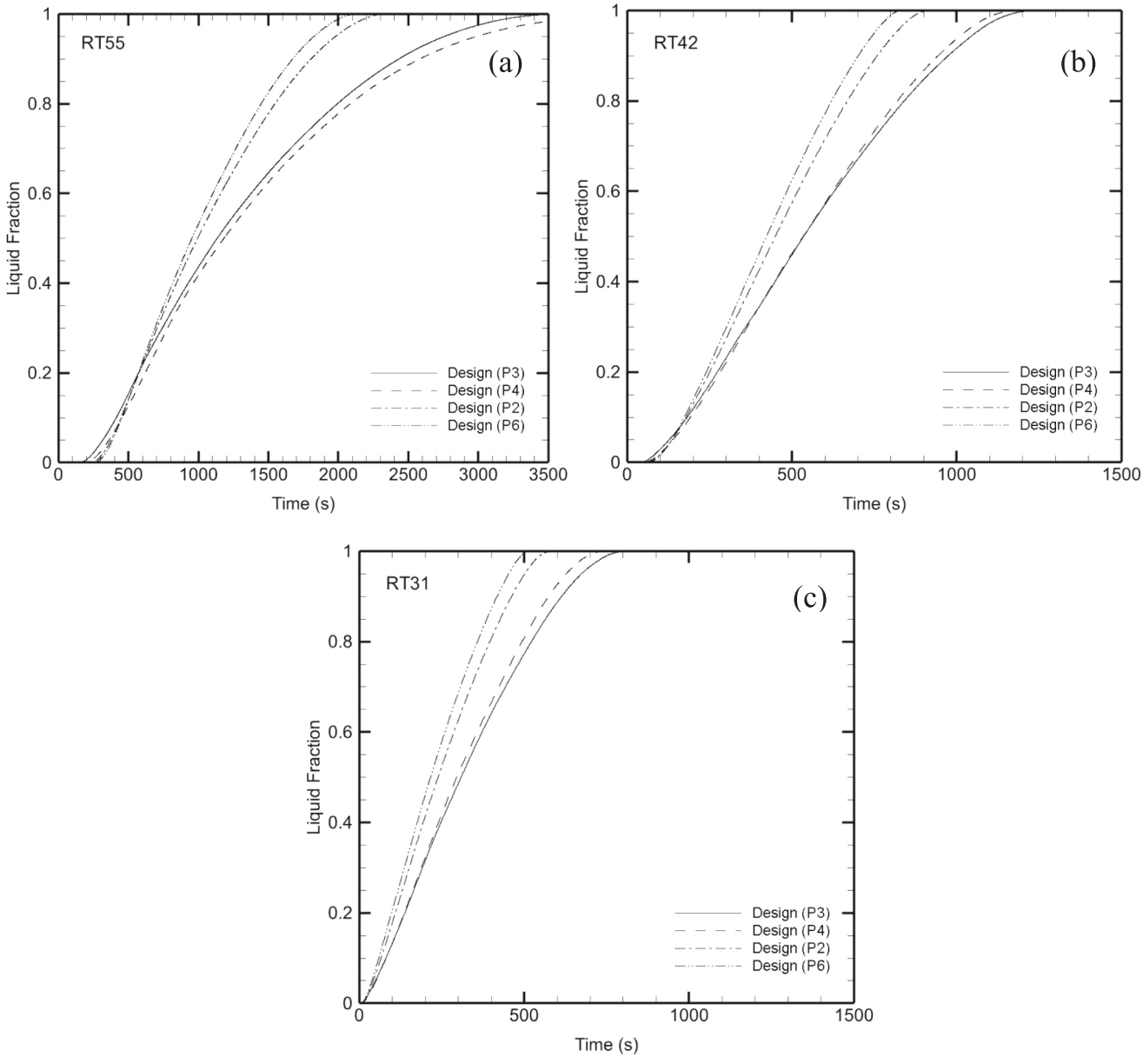

Fig. 10. Liquid fraction profiles for (a) RT55; (b) RT42; and (c) RT31.

Table 9
Time (s) to reach complete melting (LF = 1).

Design	PCM type	LF = 1
P3	RT55	3214
P3	RT42	1156
P3	RT31	751
P4	RT55	3592
P4	RT42	1113
P4	RT31	693
P2	RT55	2192
P2	RT42	875
P2	RT31	548
P6	RT55	2009
P6	RT42	802
P6	RT31	491

31 °C. This enables earlier phase change and rapid thermal buffering. P6 once again demonstrates superior performance, achieving complete melting in just 491 s, while P2 follows at 548 s. P3 and P4, owing to their design limitations, take 751 s and 693 s, respectively. The time to reach complete melting (LF = 1) for all PCM-heat sink combinations is summarized in Table 9.

5. Conclusions and future recommendation

This study numerically and experimentally investigated the thermal performance of four TPMS-based metal lattice heat sink designs octahedral (P3), waveform (P2), droplet (P4) and primitive (P6) integrated with three PCMs (RT55, RT42, and RT31) under unidirectional heat flux conditions. The results highlight the role of PCM thermal properties and lattice geometry in optimizing heat transfer and phase change dynamics for thermal management applications. Key findings include:

- The numerical predictions of base temperature were in close agreement with experimental results, showing maximum deviations of <3.7 °C for stainless steel and <2 °C for titanium configurations. This validates the numerical model's ability to accurately simulate transient heat transfer and phase change phenomena.
- Among the four TPMS designs (P3 - Octahedral, P2 - Waveform, P4 - Droplet, and P6 - Primitive), the P6 design consistently achieved the lowest base temperatures (as low as 72 °C with RT31) and shortest melting times (491 s), outperforming P2 by 28 % and P4 by over 50 %. This is attributed to its symmetrical and interconnected lattice, which facilitates efficient heat spreading and enhances natural convection.
- RT31 demonstrated the best thermal control among the three PCMs, stabilizing average temperatures approximately 5–6 °C lower than RT42 and RT55. Its lower melting point (27–33 °C) enabled earlier phase change, providing improved thermal buffering across all designs.
- The results show that performance is not solely determined by lattice or PCM alone, but by their interaction. For instance, P6 coupled with RT31 provided the best combination for fast melting and base temperature suppression, whereas P3, despite reaching higher peak temperatures, offered longer thermal storage due to its lightweight structure and higher thermal capacity.
- The findings suggest that TPMS-based metal lattices, particularly the primitive (P6) design, offer a promising approach for passive thermal management in high-heat-flux electronic applications. By selecting appropriate lattice-PCM combinations, both rapid heat dissipation and long-duration thermal buffering can be achieved, paving the way for next-generation compact heat sinks.

Future work should focus on further optimizing TPMS-based heat sinks by exploring hybrid PCM systems, where organic-inorganic combinations can enhance both heat absorption and dissipation rates. The use of functionally graded lattice structures, incorporating variations in porosity or wall thickness, could improve localized heat transfer efficiency while minimizing thermal resistances. Additionally, assessing the long-term cyclic performance of heat sinks under repeated thermal loading is essential for ensuring durability in practical applications. Experimental validation through real-time thermal imaging and flow visualization will provide deeper insights into phase change dynamics and further reinforce numerical predictions. These findings contribute to the development of advanced TPMS-PCM heat sinks for high-performance thermal management systems, offering insights into the relationship between lattice architecture and PCM properties.

CRediT authorship contribution statement

Mohammad Arqam: Writing – original draft, Methodology, Investigation, Formal analysis. **Laryssa Sueza Raffa:** Writing – original draft, Methodology, Investigation. **Matt Ryall:** Writing – original draft, Project administration, Conceptualization. **Mohammad S. Islam:** Writing – review & editing, Supervision, Investigation. **Nick S. Bennett:** Writing – review & editing, Writing – original draft, Supervision, Project administration, Funding acquisition, Conceptualization.

Declaration of competing interest

The authors declare that they have no known competing financial interests or personal relationships that could have affected the research presented in this study.

Acknowledgement

The SmartSat Cooperative Research Council and the University of Technology Sydney (UTS) jointly funded this study, with additional support provided by Romar Engineering Pty. Ltd. for the 3D printing of heat sinks. The UTS and high-performance computing facilities were utilized for experimental work and numerical modelling, respectively.

Data availability

The data will be made available upon reasonable request.

References

[1] S.M.S. Murshed, C.A. de Nieto Castro, A critical review of traditional and emerging techniques and fluids for electronics cooling, Renew. Sustain. Energy Rev. 78 (2017) 821–833.
[2] S.A.B. Al-Omari, M. Qasem, Z.A. Qureshi, E. Elnajjar, O. Al-Ketan, R.A. Al-Rub, Design and performance assessment of a triply-periodic-minimal-surface structures-enhanced gallium heat sink for high heat flux dissipation: A numerical study, Appl. Therm. Eng. 257 (2024) 124154.
[3] K. Du, J. Calautit, Z. Wang, Y. Wu, H. Liu, A review of the applications of phase change materials in cooling, heating and power generation in different temperature ranges, Appl. Energy 220 (2018) 242–273.
[4] Z.A. Qureshi, S.A.B. Al Omari, E. Elnajjar, F. Mahmoud, O. Al-Ketan, R.A. Al-Rub, Thermal characterization of 3D-printed lattices based on triply periodic minimal surfaces embedded with organic phase change material, Case Studies in Thermal Engineering 27 (2021) 101315.
[5] G. Righetti, G. Savio, R. Meneghello, L. Doretti, S. Mancin, Experimental study of phase change material (PCM) embedded in 3D periodic structures realized via additive manufacturing, Int J Therm Sci 153 (2020) 106376.
[6] Z.A. Qureshi, S.A.B. Al-Omari, E. Elnajjar, O. Al-Ketan, R.A. Al-Rub, On the effect of porosity and functional grading of 3D printable triply periodic minimal surface (TPMS) based architected lattices embedded with a phase change material, Int. J. Heat Mass Transf. 183 (2022) 122111.
[7] Y. Lin, Y. Jia, G. Alva, G. Fang, Review on thermal conductivity enhancement, thermal properties and applications of phase change materials in thermal energy storage, Renew. Sustain. Energy Rev. 82 (2018) 2730–2742.
[8] R.R. Sélo, S. Catchpole-Smith, I. Maskery, I. Ashcroft, C. Tuck, On the thermal conductivity of AlSi10Mg and lattice structures made by laser powder bed fusion, Addit. Manuf. 34 (2020) 101214.
[9] S. Catchpole-Smith, R.R.J. Sélo, A.W. Davis, I.A. Ashcroft, C.J. Tuck, A.J.A. M. Clare, Thermal conductivity of TPMS lattice structures manufactured via laser powder bed fusion, Addit. Manuf. 30 (2019) 100846.

[10] X. Hu, X. Gong, Experimental study on the thermal response of PCM-based heat sink using structured porous material fabricated by 3D printing, Case Studies in Thermal Engineering 24 (2021) 100844.
[11] Z.A. Qureshi, E. Elnajjar, O. Al-Ketan, R.A. Al-Rub, Heat transfer performance of a finned metal foam-phase change material (FMF-PCM) system incorporating triply periodic minimal surfaces (TPMS), Int. J. Heat Mass Transfer 170 (2021) 121001.
[12] K. Hosseinzadeh, E. Montazer, M.B. Shafii, A.R.D. Ganji, Solidification enhancement in triplex thermal energy storage system via triplets fins configuration and hybrid nanoparticles, J Energy Storage 34 (2021) 102177.
[13] A. Arshad, M. Jabbal, Y. Yan, Thermal performance of PCM-based heat sink with partially filled copper oxide coated metal-foam for thermal management of microelectronics, in: 2020 19th IEEE Intersociety Conference on Thermal and Thermomechanical Phenomena in Electronic Systems (ITherm), IEEE, 2020, pp. 1–8.
[14] Q. Ren, Z. Wang, J. Zhu, Z.G. Qu, Pore-scale heat transfer of heat sink filled with stacked 2D metal fiber-PCM composite, Int J Therm Sci 161 (2021) 106739.
[15] A. Chamkha, A. Veismoradi, M. Ghalambaz, P. Talebizadehsardari, Phase change heat transfer in an L-shape heatsink occupied with paraffin-copper metal foam, Appl. Therm. Eng. 177 (2020) 115493.
[16] M. Ghalambaz, J. Zhang, Conjugate solid-liquid phase change heat transfer in heatsink filled with phase change material-metal foam, Int. J. Heat Mass Transf. 146 (2020) 118832.
[17] M. Kibria, M. Anisur, M. Mahfuz, R. Saidur, I. Metselaar, A review on thermophysical properties of nanoparticle dispersed phase change materials, Energ. Conver. Manage. 95 (2015).
[18] K.Y. Leong, M.R.A. Rahman, B.A. Gurunathan, Nano-enhanced phase change materials: a review of thermo-physical properties, applications, and challenges, J Energy Storage 21 (2019) 18–31.
[19] C. Ho, Y.-C. Liu, M. Ghalambaz, W.-M. Yan, Forced convection heat transfer of Nano-Encapsulated Phase Change Material (NEPCM) suspension in a mini-channel heatsink, International Journal of Heat and Mass Transfer 155 (2020) 119858.
[20] S.E. Awan, M. Awais, M.A.Z. Raja, N. Parveen, H.M. Ali, W.U. Khan, Y. He, Numerical treatment for dynamics of second law analysis and magnetic induction effects on ciliary induced peristaltic transport of hybrid nanomaterial, Front. Phys. 9 (2021) 68.
[21] M.A. Khan, M.K. Imam, K. Irshad, H.M. Ali, M.A. Hasan, S. Islam, Comparative overview of the performance of cementitious and non-cementitious nanomaterials in mortar at normal and elevated temperatures, Nanomaterials 11 (4) (2021) 911.
[22] M. Ghaneifar, A. Raisi, H.M. Ali, P. Talebizadehsardari, Mixed convection heat transfer of Al2O3 nanofluid in a horizontal channel subjected with two heat sources, Journal of Thermal Analysis and Calorimetry 143 (3) (2021) 2761–2774.
[23] W. Usman, W. Khan, I.A. Badruddin, A. Ghaffari, H.M. Ali, Heat transfer in steady slip flow of tangent hyperbolic fluid over the lubricated surface of a stretchable rotatory disk, Case Stud. Therm. Eng. 24 (2021) 100825.
[24] S.A.B. Al-Omari, F. Mahmoud, Z.A. Qureshi, E. Elnajjar, The impact of different fin configurations and design parameters on the performance of a finned PCM heat sink, International Journal of Thermofluids 20 (2023) 100476.
[25] S.A.B. Al-Omari, Z.A. Qureshi, E. Elnajjar, F. Mahmoud, A heat sink integrating fins within high thermal conductivity phase change material to cool high heat-flux heat sources, Int J Therm Sci 172 (2022) 107190.
[26] Z.A. Qureshi, S.A.B. Al-Omari, E. Elnajjar, O. Al-Ketan, R.A. Al-Rub, Architected lattices embedded with phase change materials for thermal management of high-power electronics: A numerical study, Appl. Therm. Eng. 219 (2023) 119420.
[27] O. Al-Ketan, M. Ali, M. Khalil, R. Rowshan, K.A. Khan, R.K. Abu Al-Rub, Forced convection computational fluid dynamics analysis of architected and three-dimensional printable heat sinks based on triply periodic minimal surfaces, J. Therm. Sci. Eng. Appl. 13 (2) (2021) 021010.
[28] G. Yuandong, Y. Huning, L. Guiping, J. Haichuan, S. Xiaobin, M. Jianyin, Thermal performance of a 3D printed lattice-structure heat sink packaging phase change material, Chin. J. Aeronaut. 34 (5) (2021) 373–385.
[29] J.Y. Ho, K.C. Leong, Experimental investigation of a PCM-based topology optimized heat sink for passive cooling of electronics, in: Heat Transfer Summer Conference, American Society of Mechanical Engineers, 2020.
[30] O. Al-Ketan, M. Ali, M. Khalil, R. Rowshan, K.A. Khan, R.K. Abu Al-Rub, Forced convection computational fluid dynamics analysis of architected and three-dimensional printable heat sinks based on triply periodic minimal surfaces, Journal of Thermal Science and Engineering Applications 13 (2) (2021) 021010.
[31] S. Samson, P. Tran, P. Marzocca, Design and modelling of porous gyroid heatsinks: influences of cell size, porosity and material variation, Appl. Therm. Eng. 235 (2023) 121296.
[32] C.H. Hoang, N. Fallahtafti, S. Rangarajan, A. Gharaibeh, Y. Hadad, C. Arvin, B. Sammakia, Impact of fin geometry and surface roughness on performance of an impingement two-phase cooling heat sink, Appl. Therm. Eng. 198 (2021) 117453.
[33] A.-C. Iradukunda, A. Vargas, D. Huitink, D. Lohan, Transient thermal performance using phase change material integrated topology optimized heat sinks, Appl. Therm. Eng. 179 (2020) 115723.
[34] H.M. Ali, R.A. Lawag, T.M. Mahlia, I.M.R. Fattah, RT 42 and RT 50 phase change materials-based heat sinks for thermal management of electronics, J. Therm. Anal. Calorim. (2025) 1.
[35] T. Baig, H.A. Tariq, M. Anwar, A.A. Shoukat, H.M. Ali, M.M. Janjua, Hydrothermal performance of mini-channel heat sink using nanofluids/hybrid nanofluids: a numerical study, Energy Sources, Part A 46 (1) (2024) 4628–4646.
[36] M. Arqam, L.S. Raffa, L. Clemon, M.S. Islam, M. Ryall, N.S. Bennett, Numerical and experimental investigation of a phase change material radial fin heat sink for electronics cooling, J Energy Storage 98 (2024) 113113.
[37] L.S. Raffa, M. Ryall, N.S. Bennett, L. Clemon, Experimental investigation of the performance of a phase change material thermal management module under vacuum and atmospheric pressure conditions, Int. J. Heat Mass Transf. 236 (2025) 126384.
[38] X. Hu, X. Gong, F. Zhu, X. Xing, Z. Li, X. Zhang, Thermal analysis and optimization of metal foam PCM-based heat sink for thermal management of electronic devices, Renew. Energy 212 (2023) 227–237.